Optimized current-density reconstruction from wide-field quantum diamond magnetic field maps

Siddhant Midha,[1] Madhur Parashar,[1] Anuj Bathla,[1,2] David A. Broadway,[3] Jean-Philippe Tetienne,[3] and Kasturi Saha[1,4,5,*]

[1] *Department of Electrical Engineering, Indian Institute of Technology Bombay, Powai, Mumbai 400076, India*

[2] *Center for Research in Nanotechnology and Science, Indian Institute of Technology Bombay, Powai, Mumbai 400076, India*

[3] *School of Science, RMIT University, Melbourne, Victoria 3001, Australia*

[4] *Center of Excellence in Quantum Information, Computing Science and Technology, Indian Institute of Technology Bombay, Powai, Mumbai 400076, India*

[5] *Center of Excellence in Semiconductor Technologies (SemiX), Indian Institute of Technology Bombay, Powai, Mumbai 400076, India*

(Received 26 February 2024; accepted 5 June 2024; published 8 July 2024)

Quantum diamond microscopy using nitrogen-vacancy (N-V) defects in diamond crystals has enabled the magnetic field imaging of a wide variety of nanoscale current profiles. Intimately linked with the imaging process is the problem of reconstructing the current density, which provides critical insight into the structure under study. This manifests as a nontrivial inverse problem of current reconstruction from noisy data, typically conducted via Fourier-based approaches. Learning algorithms and Bayesian methods have been proposed as novel alternatives for inference-based reconstructions. We study the applicability of Fourier-based and Bayesian methods for reconstructing two-dimensional current density maps from magnetic field images obtained from N-V imaging. We discuss extensive numerical simulations to elucidate the performance of the reconstruction algorithms in various parameter regimes, and further validate our analysis by performing reconstructions on experimental data. Finally, we examine parameter regimes that favor specific reconstruction algorithms and provide an empirical approach for selecting regularization in Bayesian methods.

DOI: 10.1103/PhysRevApplied.22.014015

I. INTRODUCTION

Quantum-enabled magnetometry techniques provide invaluable insight into nanoscale structures by providing a spatial map of the magnetic field across the two-dimensional extent of the system. A variety of quantum systems have been shown to be viable for the quantum sensing of magnetic fields, notable examples being superconducting quantum interference devices [1–3], neutral atoms [4,5], trapped ions [6,7], and solid-state systems such as nitrogen-vacancy (N-V) centers in diamond [8–10]. Among these systems, N-V centers stand out owing to their multimodal ability to resolve changes in electromagnetic fields, temperature, and strain [11], convenient room-temperature operation and optical readout [12], and the ability to work as a single nanoscale sensor [13] or in wide-field-of-view ensemble sensing [9]. This paper focuses on reconstructing current density using magnetometry facilitated by wide-field-of-view N-V imaging or a quantum diamond microscope , employing thin layers of N-V centers embedded in bulk diamond crystals. This approach, particularly effective for large ensembles, has demonstrated per-pixel sensitivities reaching the $\mathrm{nT}/\sqrt{\mathrm{Hz}}$ level. Recently, applications such as imaging currents in microchip devices and integrated circuits [14–17], condensed matter systems [18–20], and biological systems [21,22] have been demonstrated.

The magnetic field maps obtained using quantum diamond microscopes are often utilized to compute the current density map, serving as a probe of the underlying physics in the sample under study. This reconstruction manifests as a nontrivial inverse problem. The forward problem of calculating the magnetic fields given the current density $\mathbf{j}$ across the sample is straightforward owing to the Biot-Savart law. On the other hand, the *inverse* problem is not always well defined due to added noise and imperfections in measurement, and is ill-posed owing to direct inversions involving $1/0$ terms which require additional conditioning. This leads to the possibility of different noise conditions on the same sample resulting in nonunique reconstructed images. However, it has been shown that the inverse problem of computing the current density, given

*Contact author: kasturis@ee.iitb.ac.in

the magnetic field, is unique in the case of *clean* magnetic field data produced by purely two-dimensional currents in the ideal case of infinite spatial resolution [23]. But, even with a quasi-two-dimensional current distribution, *noisy* magnetic field data superimposed with optical aberrations makes the inverse problem highly nontrivial and challenging. Owing to this nonuniqueness, many techniques have been developed to facilitate such inversions [23–31].

Traditionally, such inversion schemes deal with direct inversions in the Fourier space, as outlined by Roth *et al.* [23] for the case of out-of-plane sensing. These Fourier-based methods have been expanded to encompass vector imaging, leading to enhanced reconstructions by utilizing all available magnetic field components [24]. Recent developments in the fields of machine learning and Bayesian inference have also led to the possibility of using Bayesian methods, where the aim is to learn the most probable or "best fit" current density via maximization of the posterior probability $p(\mathbf{j}|\phi)$, where ϕ is the experimental magnetic field profile. This could be $\phi = B_z$ for the out-of-plane methods or $\phi = \{B_x, B_y, B_z\}$ for vector magnetometry. From an equivalent regularization point of view, such methods can be cast as optimization problems, where the aim is to reject the noise and retrieve the true underlying current density. At the outset, such Bayesian methods claim to offer the advantage of better reconstructions as prior knowledge about the sample can be imposed in the optimization process [26,31]. Nevertheless, there is lack of clarity on the applicability of such methods in comparison to vector and out-of-plane Fourier approaches, and no experimental advantage has been demonstrated thus far.

In this work, we conduct an in-depth comparative analysis of the Fourier-based and Bayesian reconstruction methods for both simulated and experimental magnetic maps obtained from a quantum diamond microscope where the sample is assumed to be placed at a standoff distance z from the source, as schematically outlined in Fig. 1(a). The reconstruction pipeline is further outlined in Fig. 1(b). We perform a thorough examination of the performance of reconstruction algorithms through extensive numerical simulations within various sensor regimes characterized by noise levels and standoff distances in Sec. II. Following this, in Sec. III we build on our theoretical analysis by exploring practical approaches for determining the regularizer strength in Bayesian algorithms, and applying them to experimental data collected in three different noise and standoff scenarios. Through this, we introduce the concept of Bayesian advantage in the realm of current density reconstructions for N-V wide-field experiments.

II. SIMULATION RESULTS AND DISCUSSIONS

As a test structure, we use a microcoil wire—carrying a purely two-dimensional current to model a quasi-two-dimensional flow—with multiple sharp bends to effectively highlight nuances of reconstruction algorithms. A comprehensive outline of the simulation method, which includes the process for computing magnetic fields from current densities, as well as a detailed explanation of the reconstruction methodology is provided in the Supplemental Material [32]. The assumed true current density, which by definition forms the ground truth, is depicted in Fig. 1(c), where we define the j_x and j_y components of the spiral wire piecewise in a total image size of $50 \times 50\ \mu\text{m}^2$. The scale bar in Fig. 1 is 10 μm. We assume a constant current density of 100 A/m across the wire. The resulting magnetic field, computed at a standoff of $z = 1\ \mu$m, using a Fourier-space application of the Biot-Savart kernel $\mathcal{M}$, is shown in Fig. 1(d).

Reconstruction algorithms have access to one or more components of the magnetic field, as in Fig. 1(d), and attempt to decode the underlying current density. The Fourier-XY ($\mathcal{F}_{XY}$) method takes as input the x- and y-components of the magnetic field, and performs a Fourier space inversion for the current density. The Fourier-Z ($\mathcal{F}_Z$) performs this task with access only to the out-of-plane z-component. Lastly, we consider the Bayesian ($\mathcal{B}$) class of methods, which cast the inversion problem as inference, and solve it by performing Bayesian optimization. We consider a scenario in which the Bayesian algorithm has only the out-of-plane field component as input, emphasizing its effectiveness in situations with limited data, and simultaneously conducting a worst-case comparison with the Fourier-XY method. Intuitively, the task of finding the most probable current density can be converted into an optimization consisting of two terms: the first terms tries to fit to the data, and the second term attempts to create a smooth solution. The latter, termed a *regularizer*, can be used to incorporate prior information about the current density into the optimization. A parameter λ defines the strength of the regularizer, where a very small value $\lambda \to 0$ amounts to data fitting, and a very large value $\lambda \to \infty$ results in oversmoothened solutions. Thus, the regularizer strength λ is a crucial part of the Bayesian reconstructions, and is used to ensure smooth and physical reconstructions.

The reconstructed j-maps, upon application of both the Fourier and Bayesian methods on the magnetic images in Fig. 1(d), are shown in Fig. 1(e). The regularizer strength $\lambda = \lambda^*$ is carefully selected in the Bayesian method, following a systematic and experimentally informed procedure that we outline in the Supplemental Material [32]. In the rest of the simulation results, we perform the comparative analysis of the Bayesian method in a nonadaptive setting *without* performing regularizer selection, to outline worst-case behavior. The following three subsections outline the analysis of the three reconstruction algorithms on the simulated data in various noise and standoff regimes.

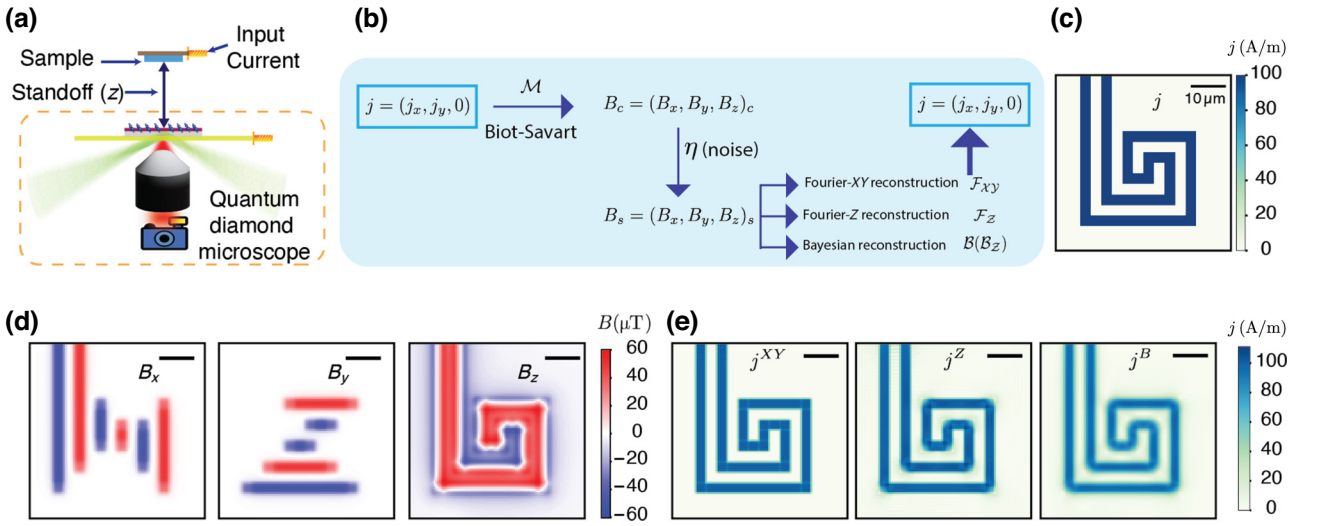

FIG. 1. (a) Schematic of quantum diamond microscope with a sample placed at a standoff distance denoted by z. (b) Block diagram of the simulated reconstruction protocol: the clean magnetic field $\mathbf{B}_c$ is computed from the current density $\mathbf{j}$ via the Biot-Savart kernel $\mathcal{M}$, followed by addition of noise η to get the sensed fields $\mathbf{B}_s$. Subsequent postprocessing steps using the Fourier-XY ($\mathcal{F}_{XY}$), the Fourier-Z ($\mathcal{F}_Z$), and the Bayesian ($\mathcal{B}$) methods result in different reconstructed current densities $\hat{\mathbf{j}}$. (c) Simulated spiral wire current density map. (d) Vector magnetic field maps computed from the current density without noise ($\eta = 0$) at a standoff of $z = 1$ μm. (e) Reconstructed current density upon application of the three algorithms on the field data.

A. The effect of standoff

The distance between the sample and the N-V sensor, or the "standoff" (z), is a key parameter that strongly affects the measured magnetic field maps and consequently the underlying current distribution. This can be seen from the exponential dependence on standoff distance in the Biot-Savart kernel, $\mathcal{M}$ [32]. This underscores the need for a thorough analysis of how the performance of the algorithms is influenced by the standoff distance.

We plot two error-estimation metrics, the two-normed distance (D_{L2}) and the structured similarity index (SSIM), first introduced in [33], as a function of standoff z in Figs. 2(a) and 2(b) respectively, without any added noise ($\eta = 0$). See [34,35] for brief reviews of the error and similarity metrics. The two-normed distance measures the Euclidean distance between two images, and the SSIM measures a "score" of visual similarity [32]. The Bayesian reconstructions require selecting the strength of a *regularizer* term, which maintains smoothness of the reconstructed solution. Here, we do not perform systematic regularizer selection and rather choose three fiducial strengths $\lambda \in \{0.01, 0.1, 1\}$ in a *nonadaptive* fashion. The Fourier methods, on the other hand, require choosing a cut-off frequency to band-limit the spectrum and perform inversions [32]. We perform adaptive Fourier reconstructions ($\mathcal{F}_{XY}$, $\mathcal{F}_Z$) with the cutoff frequency of the algorithms changing with every 2-μm increase in standoff, as elaborated in [32]. Two points representing the low standoff $z_1 \lesssim 1$ μm and high standoff $z_2 \gtrsim 5$ μm are marked in the error plots with dotted lines. First, we observe that in both D_{L2} and SSIM, the Fourier-XY method ($\mathcal{F}_{XY}$) performs better for the low-standoff regime of $z \lesssim 1$ μm. As the standoff is increased, there exists a critical point beyond which the Bayesian method ($\mathcal{B}$) method starts to outperform $\mathcal{F}_{XY}$. This can be explained by noting that the $\mathcal{F}_{XY}$ method is exact at low standoff, eliminating aberrations due to its ability to access both in-plane components; however, the spiral wire contains a nontrivial frequency spectrum owing to multiple sharp corners, and thus requires a careful selection of a band-limiting frequency for the Fourier algorithms at higher standoff. Additionally, without such a selection of the cutoff frequency in the Fourier algorithms at higher standoffs, high-frequency artifacts dominate the Fourier reconstruction. This leads to a sharp unbounded increase in the D_{L2} metric at $z \approx 8$ μm. In contrast, the Bayesian reconstruction exhibits an SSIM decrease of less than 10% for standoff distances of $z \lesssim 5$ μm.

Figures 2(c) and 2(d) show reconstructed current densities at $z = 0.95$ μm and $z = 5.7(5)$ μm standoff, respectively. At $z = z_1$ in Fig. 2(c), none of the reconstructions show any artifacts, and resolve the widths of all the arms correctly. The Bayesian images show an offset above the true value, which is attributed to the fact that the regularizer strengths are chosen arbitrarily. In Fig. 2(d), when the standoff is increased, noticeable discrepancies in the Fourier images become apparent, including an offset and a notable decline in resolution. However, the Bayesian image, particularly with $\lambda \lesssim 0.1$, exhibits a significantly improved outcome. It is instructive to note that the Bayesian image with $\lambda = 1$ is significantly broadened,

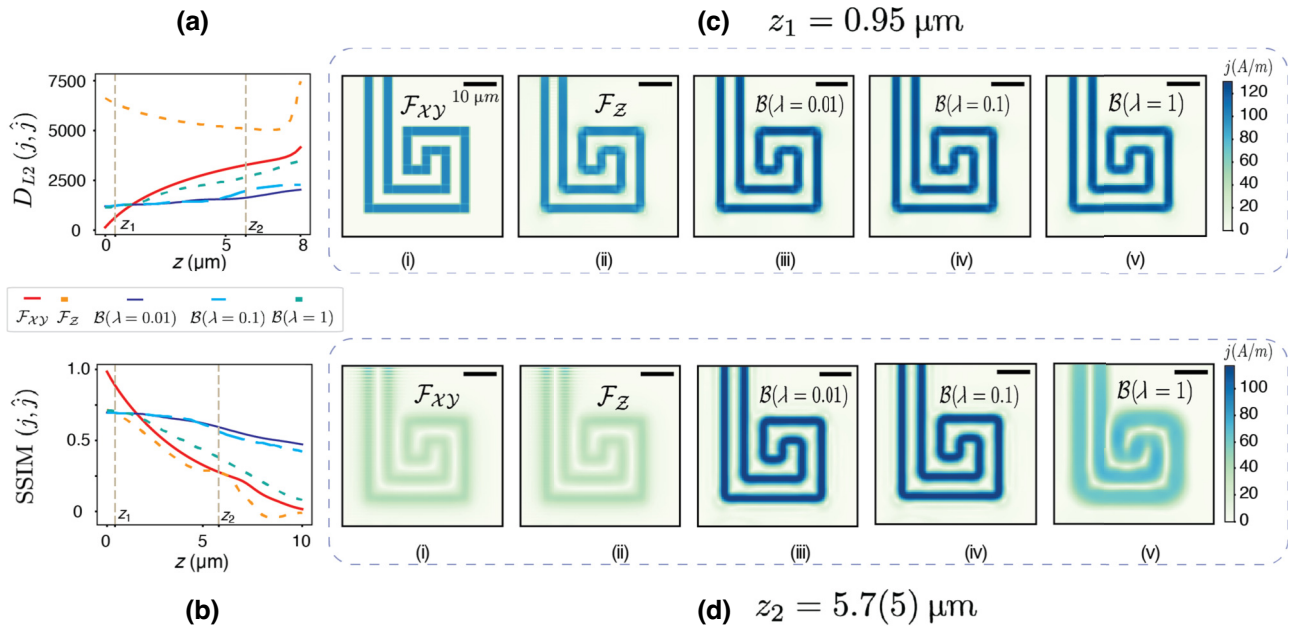

FIG. 2. Performance of the reconstruction algorithms as a function of the standoff distance in terms of the distance D_{L2} and the structured similarity index (SSIM) between the reconstructed and true current densities. (a) D_{L2} as a function of standoff for $0 \leq z \leq 8$ μm. (b) The SSIM as a function of standoff for $0 \leq z \leq 10$ μm. Two standoff points $z_1 = 0.95$ and $z_2 = 5.7(5)$ (all in micrometers) are identified for further inspection. (c) Reconstructions at $z = z_1$. (d) Reconstructions at $z = z_2$. The subpanels of (b),(d) show the reconstructions for Fourier-*Z* and the Fourier-*XY* methods (with a Fourier cutoff frequency of $\max\{2, \text{int}(z(\mu\text{m}))\}/z$) and the Bayesian reconstruction for three different regularizer strengths $\lambda \in \{0.01, 0.1, 1.0\}$.

which is attributed to the oversmoothening in the optimization process owing to a larger regularizer strength than required. Both the Fourier and Bayesian algorithms necessitate the fine-tuning of parameters within a fixed set of fields ϕ, either through the specification of a band-limiting frequency or the adjustment of a regularizer strength. It is crucial to highlight that achieving precise fine-tuning in the Fourier method becomes challenging at higher standoffs, particularly when dealing with nontrivial frequency spectra, and no systematic method exists for such tuning in the Fourier methods. Additionally, the results presented in Fig. 2 indicate the strict requirement for tuning of parameters for the Fourier method as the standoff increases, contrasting with the Bayesian method, which requires minimal tuning, and $\mathcal{B}(\lambda \lesssim 0.1)$ consistently yields high-quality reconstructions as the standoff increases. It is noteworthy that while the D_{L2} in Fig. 2(a) method exhibits a substantial difference in the performance of $\mathcal{F}_{XY}$ and $\mathcal{F}_Z$, particularly around $z \approx z_1$, the reconstructions depicted in Fig. 2(c) showcase similar performance of the two methods. The structural similarity index effectively reflects this observation, emphasizing that the SSIM distance provides more perceptual information regarding the algorithms' performance compared to the two-normed distance. Consequently, the SSIM, being constrained by the condition SSIM$\leq$1, is considered a superior metric. In the rest of the paper, we use the SSIM exclusively for quantifying the error, resulting in a bounded, well-informed estimation metric.

B. Robustness to noise

We now study the effect of noise on reconstruction. We employ two noise models—Gaussian noise, which distributes across the entire image uniformly, and *scaled noise*, which is more prominent at pixels with higher absolute values. Both the models add zero-mean Gaussian noise to each pixel, with the former having a pixel- independent variance and the latter having a variance that scales with the absolute value of the pixel. The amount of noise in both models is controlled by a single parameter η [32]. We study the SSIM distance between the reconstructed and ground-truth current densities as a function of noise strength η. Results are shown here for Gaussian noise, with scaled noise exhibiting similar patterns—differences between the two noise models are shown in the next subsection. Figure 3 shows the results for the low-standoff regime of $z = 0.1$ μm and the high-standoff regime of $z = 5$ μm. For Bayesian reconstructions, $\lambda \in \{0.1, 1.0\}$ is chosen. The $\lambda = 0.01$ case is omitted as the presence of noise warrants nontrivial regularization. In the scenario with a low standoff, the $\mathcal{F}_{XY}$ method emerges as the most effective, displaying the highest SSIM score for the entire noise range $0 \leq \eta_g \leq 2$. The SSIM also

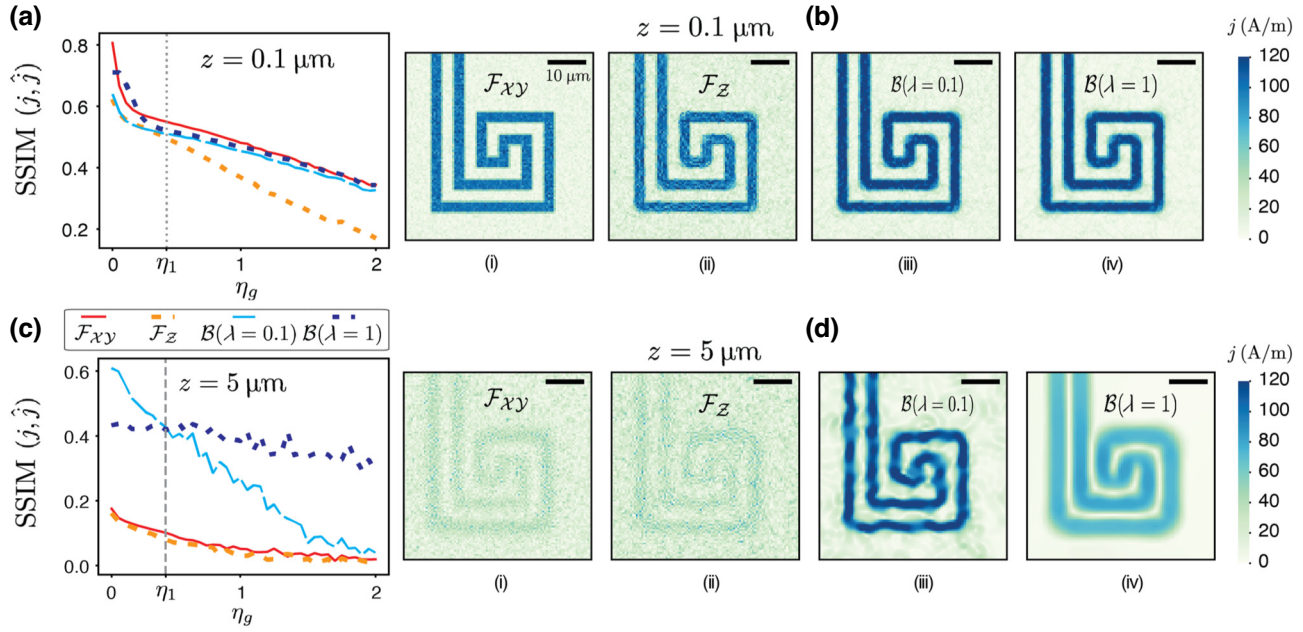

FIG. 3. Analyzing the effect of noise on the reconstructions using the SSIM as the error metric. (a),(b) Results for the low-standoff regime of $z = 0.1$ μm. (c),(d) Results for the high-standoff $z = 5$ μm regime. The SSIM as a function of Gaussian noise η_g is reported in (a),(c) for the two regimes, while (b),(d) show the Fourier and Bayesian reconstructions at the $\eta_1 = 0.45$ noise level as marked with a dotted line. The Bayesian reconstructions are shown for two regularizer strengths $\lambda \in \{0.1, 1.0\}$.

reveals two distinct patterns at low standoff — a rapid decline in algorithm performance with increasing noise, followed by a shift in slope after reaching a critical noise strength. This phenomenon can be linked to a critical signal-to-noise (SNR) ratio, where the noise levels equate to the signal strength, resulting in two performance regimes. The $\mathcal{F}_Z$ image exhibits a low SNR ratio within the wire, leading to diminished SSIM as noise levels escalate. In contrast, the $\mathcal{B}(\lambda)$ reconstructions exhibit high SNR, as well as the characteristic offset associated with the lack of regularizer selection.

The outcomes for the high-standoff regime are depicted in Figs. 3(c) and 3(d). The SSIM plot indicates a consistent score (SSIM≈0.4) performance for the $\mathcal{B}(\lambda = 1)$ reconstructions, and reveals intriguing behavior for $\mathcal{B}(\lambda = 0.1)$. The $\lambda = 0.1$ approach surpasses all other reconstructions until reaching $\eta_1 = 0.45$, after which it exhibits a score lower than the $\lambda = 1$ reconstruction. This phenomenon can be explained as follows. At minimal noise levels, the appropriate regularizer strength is closer to $\lambda \sim 0.1$, resulting in accurate resolution and noise rejection. Subsequently, in this high-standoff scenario, with increasing noise, there is a swift change in the required regularizer strength, leading to a rapid decline in performance. This analysis is extended by presenting the reconstructed densities at $\eta = \eta_1$ in Fig. 3(c) for this case. The $\mathcal{B}(\lambda = 0.1)$ reconstruction correctly resolves the wire but exhibits substantial spurious noise outside the wire, as anticipated due to the crossover at $\eta = \eta_1$. In other words, the consistent performance of the $\lambda = 1$ method stems from the fact that the regularizer strength is much larger than the optimal value, resulting in effective noise rejection but significant broadening overall. The optimal value of the regularizer lies between the two extremes depicted. On the other hand, the Fourier $(\mathcal{F}_{XY}, \mathcal{F}_Z)$ reconstructions show a very small and decreasing similarity score SSIM$\lesssim$0.2, as can be seen from the reconstructions in Fig. 3(d).

Therefore, we deduce that under conditions of very low standoffs and moderate noise, the $\mathcal{F}_{XY}$ approach stands out as a promising option for wide-field reconstructions when provided with access to all in-plane measurement data. In scenarios where only out-of-plane data are available, the $\mathcal{B}$ method demonstrates comparable or superior performance compared to $\mathcal{F}_Z$ at low standoffs. As standoff distances increase, the utilization of Bayesian techniques becomes imperative, with the $\mathcal{B}$ method consistently outperforming $\mathcal{F}_Z$ across all noise levels, even without the need for regularizer tuning for moderate noise levels $\eta \lesssim \eta_1$. It is important to note that the distinction between low- and high-standoff scenarios is representative and may be influenced by factors such as wire length-scales relative to image length and the amount of current in the wire, impacting the SNR. The selection of a high current density magnitude of 100 A/m allows these two regimes to be delineated at $z \in \{0.1, 5\}$ μm, which can be realized by varying the standoff in experimental settings.

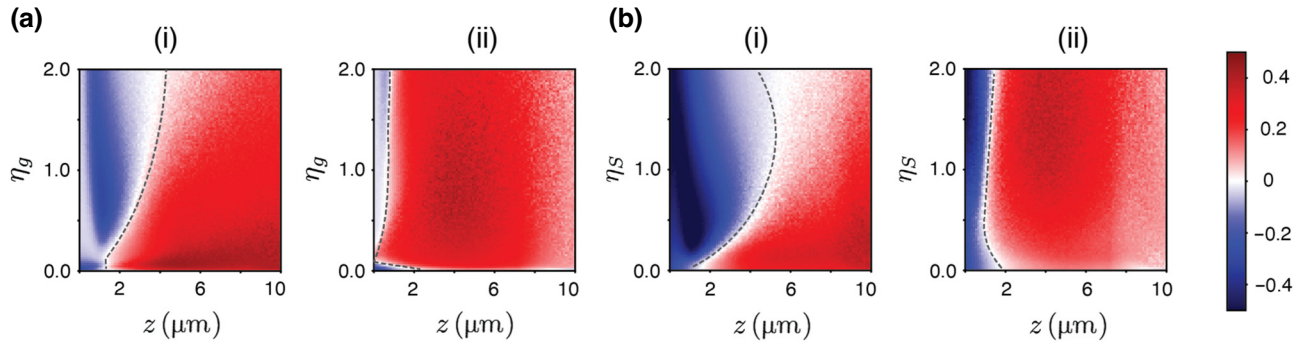

FIG. 4. Phase diagram of Bayesian advantage. The SSIM metric for the Bayesian and Fourier-*XY* reconstructions with the true densities is computed as a function of the standoff z and the noise level η, and their difference is shown. (a) Results for Gaussian noise. (b) Results for scaled noise. Subpanels are for regularizer strengths (i) $\lambda = 0.1$ and (ii) $\lambda = 1.0$. The red and blue regions represent Bayesian and Fourier advantage, respectively, and the dotted line marks the phase transition boundary.

C. Phase diagram

We now investigate the combined effects of η and z to define and demonstrate *Bayesian advantage*. The standoff and the noise are varied in the ranges $z \in [0, 10]$ μm, and $\eta_{g/s} \in [0, 2]$, respectively. To quantify Bayesian advantage, we construct a map of the SSIM distance as a function of η and z for the $\mathcal{B}$ and $\mathcal{F}_{XY}$ methods and define

$$d(z, \eta) := \mathrm{SSIM}(z, \eta; \mathcal{B}) - \mathrm{SSIM}(z, \eta; \mathcal{F}_{XY}), \quad (1)$$

where $\mathrm{SSIM}(z, \eta; \mathcal{X})$ denotes the SSIM computed in the case of standoff z, noise η, and the algorithm $\mathcal{X} \in \{\mathcal{B}, \mathcal{F}_{XY}\}$. Note that $-1 \leq d(z, \eta) \leq 1$, where $d > 0$ and $d < 0$ indicate Bayesian and Fourier-*XY* advantage, respectively. The Fourier-*XY* method is chosen as a comparative candidate of Bayesian advantage owing to its superior performance in the Fourier methods, and parameters for both the algorithms are held constant.

The outcomes for $d(z, \eta)$ are presented in Fig. 4 for (a) Gaussian and (b) scaled noise, with subpanels illustrating the model selection for the Bayesian approach using $\lambda \in \{0.1, 1\}$ in accordance with the earlier discussions. The dashed line signifies a distinctive *phase transition* (in the spirit of similar phase diagrams in optimization dynamics; see, for instance, [36]) from Fourier to Bayesian advantage, for which $d(z, \eta)$ serves as an effective order parameter. In the case of Gaussian noise in Fig. 4(a), results indicate that at very low standoffs, there is no clear preference for either of the two methods, as was seen in Fig. 3(a). Additionally, for $\lambda = 1$ in the Bayesian scenario, the Fourier advantage region diminishes, suggesting that adequate regularization in Bayesian optimization generally leads to improved reconstruction quality without the need for regularizer tuning. In the case of scaled noise in Fig. 4(b), similar to a "phase transition," the results show a notable contrast with a pronounced Fourier advantage at low standoffs, as evidenced by the image contrast. Moreover, the area of Fourier advantage is smaller in the Gaussian noise case [Fig. 4(a)] than in the case of scaled noise [Fig. 4(b)]. This is because Gaussian noise has a flat and nondecaying spectrum for any $\eta_g > 0$, playing a more detrimental effect in Fourier inversions.

Given the consistent Bayesian advantage in the presence of Gaussian noise, employing an adaptive regularizer scheme would theoretically yield a $d(z, \eta)$ plot that is consistently positive. Furthermore, these findings indicate that a significant portion of the experimental scenarios (quantified here as the η-z plane) demonstrate the Bayesian advantage. This necessitates a thorough discussion of such Bayesian protocols on experimental data, which is conducted in the following section.

III. RECONSTRUCTION FROM EXPERIMENTAL MAGNETIC MAPS

In the previous discussions, we demonstrated how inference-based protocols exhibit an advantage in current-density reconstruction by studying simple uncorrelated noise. In this section, we further show that the same models indeed work on experimental data, presumably incurring nonanalytical and correlated noise, and further exemplify the Bayesian advantage. We now apply the reconstruction algorithms to three chosen experimental scenarios to illustrate the points described via simulations in the previous section. The regularizer selection—the search for the optimal tradeoff λ^*—for Bayesian reconstructions on the experimental data is performed using the *l*-curve method and via an analysis of the total integrated currents. The *l*-curve method involves searching for a bending point in a parametrized plot of the norm of the reconstructed density $||\hat{j}_{\mathcal{B}}||_2$ against the norm of the residual $||\mathcal{M}(\hat{j}_{\mathcal{B}}) - B_c||_2$ as the λ parameter is varied (see [37,38]). The key idea behind selecting a near-optimal regularizer is to include correct prior information about the expected current densities in the optimization process. Mathematically, we enforce a particular functional form, known as the

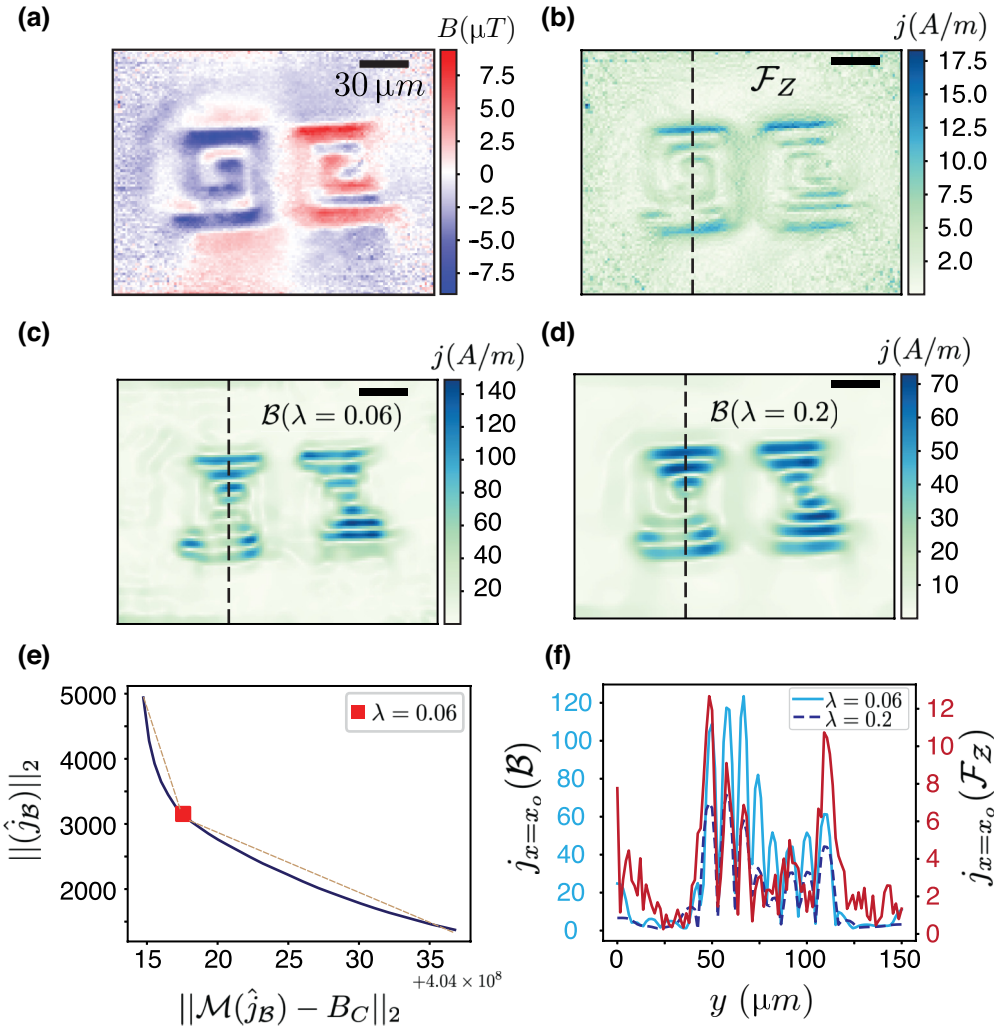

FIG. 5. Analysis of the microspiral wire. (a) Experimentally acquired magnetic field map projected along a given N-V axis, with an estimated standoff of $z \sim 5$ μm. (b) Reconstruction performed using the Fourier-Z ($\mathcal{F}_Z$) method. (c),(d) Bayesian reconstructions for two different regularizer strengths $\lambda \in \{0.06, 0.2\}$ respectively. The dotted line marks the point $x_0 = 68$ μm in the reconstructions. (e) l-curve showing a turn at $\lambda = 0.06$. (f) Line-cut plots along the dotted line at $x = x_0$. Scale bars are 30 μm.

total-variation regularizer [39,40], which ensures smoothness of the reconstruction by penalizing the first derivatives. The strength of this prior is then controlled by the parameter λ. A small $\lambda \approx 0$ fits to the data, which can include the noise, and will produce exactly the same results as the Fourier inversion in the case of no noise ($\eta = 0$). The ingenuity of the Bayesian methods lies in tuning the λ, to be able to control the tradeoff between fitting the exact noisy data and rejecting the noise to reconstruct the correct fields. Details of the regularizer selection method are outlined with the simulated microcoil wire as an instructive example in the Supplemental Material [32].

A. Microspiral wire

The microspiral wire consists of two spiral coils placed next to each other, carrying currents of opposite polarity. The magnetic field image of the microspiral obtained through N-V wide-field imaging is shown in Fig. 5(a). We note that a lack of contrast at the left- and rightmost arms of the wire is present owing to imperfections in the imaging. We reconstruct the current density maps via $\mathcal{F}_Z$ and $\mathcal{B}$ using the out-of-plane B_z-component of the magnetic field.

The Fourier reconstruction is displayed in Fig. 5(b), and the Bayesian reconstructions for regularizer strengths $\lambda \in \{0.06, 0.2\}$ are depicted in Figs. 5(c) and 5(d), respectively. A dashed line is positioned at $x_0 = 68$ μm for further investigation through line-cuts. The selection of $\lambda = 0.06$ is determined from the l-curve illustrated in (e), where the turning point is identified by the asymptotic lines drawn. The challenging balance between data fitting and noise rejection, given the wire's current of 500 μA, a high standoff of approximately 5 μm, and noise in the image leads to a clear distinction between two asymptotic regimes.

Upon closer inspection, the Fourier image reveals numerous spurious currents outside the wire region, reaching up to 50% of the maximum value. Additionally, there is a noticeable loss of resolution in the inner arms of the wire in the Fourier image, particularly along the $x = 68$ μm dotted line. Furthermore, the magnitude of the Fourier image is inaccurate, resulting in a total integrated current of 503(4) μA at the $x = 68$ μm line, significantly deviating from the expected value of $8 \times 500 \sim 4000$ μA due to the wire's eight arms. In contrast, the Bayesian reconstruction for $\lambda = 0.06$ exhibits precise resolution of the inner arms, with the left- and rightmost arms remaining unresolved. The total integrated current at $x = 68$ μm is 4320(6) μA, aligning with the expected 4000 μA value. With a larger strength of $\lambda = 0.2$, fewer noise artifacts are observed outside the wire, but the wire's width increases, resulting in a total current of 2661(5) μA. However, due to increased regularization, this reconstruction offers improved resolution of the left- and rightmost arms.

Line-cut plots along the dashed line of the current maps at the position $x = 68$ μm elucidate these observations. The $\mathcal{B}$ cuts exhibit sharper resolution of the arms and less noise outside the wire region. The resolution of the $\mathcal{B}(\lambda = 0.06)$ line-cut is particularly evident, while the $\mathcal{F}_Z$ plot displays reduced resolution of the arm at $y = 100$ μm and an inaccurate magnitude of the density. Given the noise and standoff conditions, the $\mathcal{B}(\lambda = 0.06)$ reconstruction emerges as the most favorable in the microspiral wire.

B. Niobium wire

In contrast to the microspiral wire with large noise and standoff, we now investigate the reconstruction algorithms on a Nb wire [24], as shown in Fig. 6, carrying a high total current of 20 mA leading to a high SNR, with a low standoff of $z \sim 0.1$ μm and a large wire-length to image-length ratio. This experiment represents the polar opposite case of the microspiral wire. According to the simulations and as per the phase diagram analysis, we expect no Bayesian advantage in this experiment. The vector magnetic field maps are shown in Fig. 6(a). We observe that in the B_z map the field at the top and bottom edges of the image is not fully decayed, being still around 25% of the maximum values, which is expected to cause artificial edge currents in the $\mathcal{F}_Z$ reconstructions due to data truncation. We also note the presence of a physical defect in the magnetic images in a region around the point $x = y = 45$ μm (from the bottom-left corner).

The reconstructions utilizing the $\mathcal{F}_{XY}$ and $\mathcal{F}_Z$ methods are respectively depicted in Fig. 6(b)(i),(ii). The $\mathcal{F}_{XY}$ illustrates an immaculate reconstruction, featuring a distinct identification of the defect in the fields, absence of noise artifacts, and a total integrated current of 20 mA at $x = x_1$

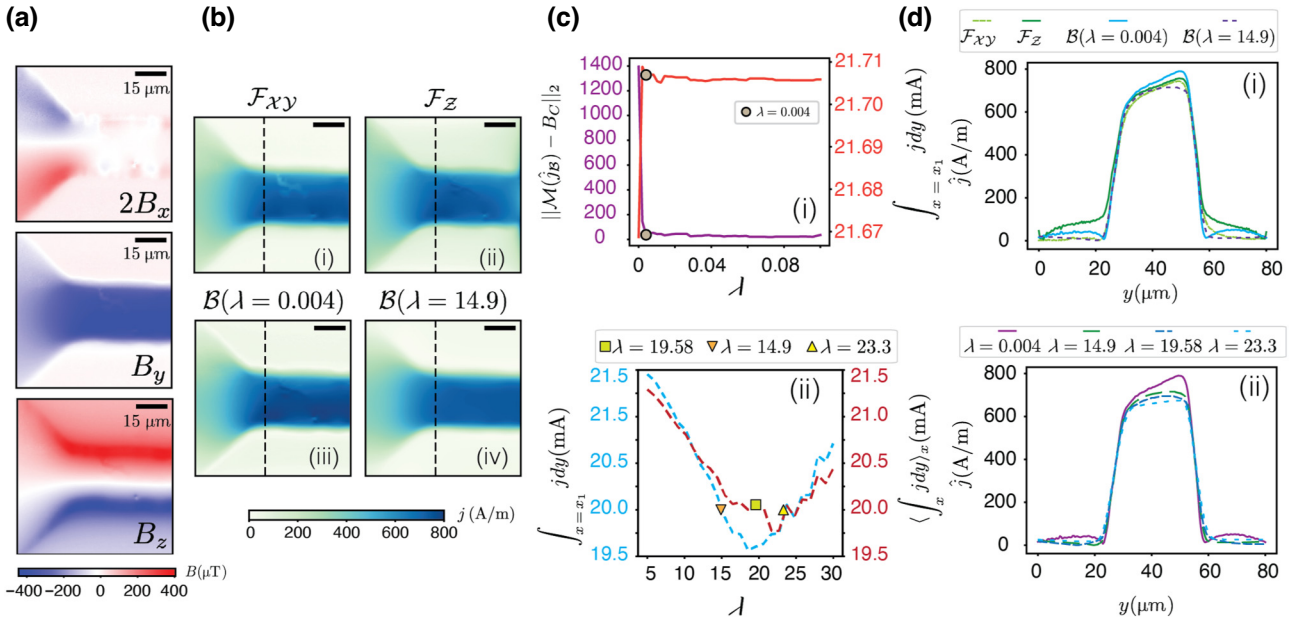

FIG. 6. Analysis of the niobium wire. (a) Magnetic field data obtained from N-V wide-field imaging on the Nb wire, with a standoff $z \sim 0.1$ μm. Data are taken from Ref. [24]. (b) Reconstructed current densities using the Fourier-XY and Fourier-Z methods, and Bayesian reconstructions for $\lambda \in \{0.004, 14.9\}$ with a dotted marked line at $x_1 = 36$ μm. (c)(i) The magnetic field two-norm distance (left axis) and the total integrated current at $x = x_1$ (right axis) for small regularizer strengths $0 \leq \lambda \leq 0.1$. (c)(ii) The current at $x = x_1$ (left axis) and the total averaged integrated current (right axis) for large regularizer strengths $5 \leq \lambda \leq 30$. (d)(i) Line-cut plots of the density maps for the Fourier and Bayesian $\lambda \in \{0.004, 14.9\}$. (d)(ii) Line-cuts for Bayesian reconstructions with different regularizer strengths $\lambda \in \{0.004, 14.9, 19.5(8), 23.3\}$. Scale bars are 15 μm.

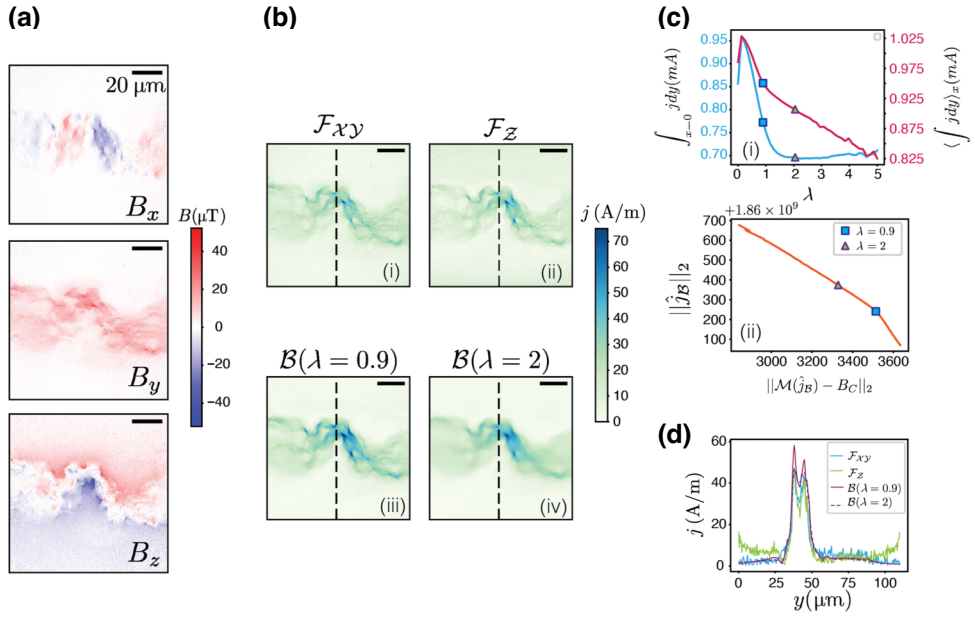

FIG. 7. Analysis of the graphene wire. (a) Magnetic field data obtained from N-V wide-field imaging on the graphene device, with a standoff of $z \sim 20$ nm. Data are taken from Ref. [17]. (b) Reconstructed density magnitudes using the Fourier and the Bayesian method by using $\lambda \in \{0.9, 2\}$ with $x_2 = 54$ μm marked with a dotted line. (c)(i) Total integrated current entering from the left at $x = 0$ (left axis) and average value of the total integrated currents (right axis) with $\lambda \in \{0.9, 2\}$ marked. (c)(ii) l-curve showing a turn at $\lambda = 0.9$. (d) Line-cut plots along the dotted line at $x = x_2$. All scale bars are 20 μm.

(indicated by the dotted line in the reconstructions). In contrast, the $\mathcal{F}_Z$ image is derived after subtracting bias to address artifacts induced by truncation effects, albeit still exhibiting some edge artifacts towards the right of the image. The total current in this case is 21(8) mA, deviating from the expected value of 20 mA.

The Bayesian reconstructions are respectively displayed in Fig. 6(b)(iii),(iv) for the regularizer strengths $\lambda \in \{0.004, 14.9\}$. The selection of $\lambda = 0.004$ is determined from a plot of the residual norm $||\mathcal{M}(\hat{j}_\mathcal{B}) - B||_2$ and the total current at $x = x_1$ as functions of λ, illustrated in Fig. 6(c)(i) for small regularizer strengths $\lambda \leq 0.1$. With an increase in regularizer strength, critical points emerge in both the total current at $x = x_1$ and the averaged total currents, as depicted in Fig. 6(c)(ii) for λ. Owing to the absence of sufficient noise to indicate a turning point in the l-curve, it is not shown here. The significant λ points in $\{14.9, 19.58, 23.3\}$ exhibit similar reconstruction features; thus, the reconstructed image for $\lambda = 14.9$ is presented, where both the average current and the current at $x = x_1$ align at approximately 20 mA. It is noteworthy that the $\mathcal{B}(\lambda = 0.004)$ reconstruction reveals sharper underlying features, such as the defect, reporting a current of 21(7) mA at x_1. In contrast, the $\mathcal{B}(\lambda = 14.9)$ image, influenced by the large regularizer, averages out finer features but reports a current of 20(1) mA at $x = x_1$. This emphasizes that the l-curve method is not always applicable in experimental scenarios where the fitting and smoothening regimes are difficult to delineate, and thus an analysis of the total integrated current and residual magnetic field errors must be conducted in order to select $\lambda \approx \lambda^*$. The line-cut plot in Fig. 6(i) elucidates this point, and Fig. 6(ii) shows the subtle difference between the Bayesian reconstructions for different regularizer strengths. While the $\mathcal{B}$ reconstructions show no edge artifacts and are superior to the $\mathcal{F}_Z$ images, the $\mathcal{F}_{XY}$ method emerges superior owing to this difficulty in the Bayesian trade-off.

C. Graphene wire

Finally, we apply the reconstruction algorithms on imaging of a graphene wire using wide-field N-V imaging [17]. The standoff is again low ($z \sim 20$ nm) but the current pattern is much more complex than in the Nb-wire case. The results are shown in Fig. 7. The vector magnetic field maps are shown in the three panels of Fig. 7(a). Before discussing the results, we note that the total current flowing from the source (left) into the graphene channel is 700 μA which, along with the fine features of the graphene wire, implies a low SNR in the image.

The reconstructions for the $\mathcal{F}_{XY}$ and $\mathcal{F}_Z$ cases are depicted in Fig. 7(b)(i),(ii), while the outcomes for the $\mathcal{B}$ algorithm, employing two different regularizer values, $\lambda \in \{0.9, 2.0\}$, are illustrated in Fig. 7(b)(iii),(iv). A dotted line at $x_2 = 53(5)$ μm serves as a reference point for subsequent line-cut analyses, as shown in Fig. 7(d). The plots pertaining to regularizer selection for the $\mathcal{B}$ method are presented in Fig. 7(c).

Upon visual examination, the reconstructions of the $\mathcal{F}_{XY}$ and $\mathcal{F}_Z$ cases exhibit notable similarity, with moderate edge artifacts apparent in the $\mathcal{F}_Z$ reconstruction. This outcome aligns with expectations, as the magnetic field B_z experiences significant decay towards the top and bottom sides of the sample image, resulting in minimal truncation artifacts. However, both Fourier reconstructions display considerable Gaussian noise, evident in the density maps and the total integrated current at $x = 0$, measuring 956(7) μA for $\mathcal{F}_{XY}$ and 1271(4) μA for $\mathcal{F}_Z$. Both values deviate significantly from the anticipated 700 μA.

In contrast, the Bayesian reconstructions do not exhibit Gaussian noise outside or on the wire, although the $\lambda = 0.9$ reconstruction displays minor aberrations beyond the wire region, which are observed to diminish in the $\lambda = 2$ case. The choice of $\lambda = 0.9$ was determined from the turn in the *l*-curve shown in Fig. 7(d)(i), yet the total integrated current at $x = x_2$ reaches 700 μA at $\lambda = 2$ [Fig. 7(d)(ii)]. While the total current at x_2 and the total average current, plotted in the two axes of Fig. 7(d), both converge to approximately 700 μA at a higher strength of $\lambda = 4.7$, the reconstruction at such high regularization appears excessively smoothed, lacking the finer details of current flow in the wire. Additionally, the $\lambda = 0.9$ reconstruction reports a total entering current of 772 μA—showing significantly less deviation than the Fourier methods—while the $\lambda = 2$ reconstruction shows an entering current of 695(7) μA. This further underscores that the *l*-curve, when combined with the total current, offers a reliable method for selecting the appropriate regularization in Bayesian algorithms for wide-field imaging scenarios. The line-cut plots in Fig. 7(e) support this analysis by illustrating (1) the edge artifacts in the $\mathcal{F}_Z$ case, (2) noise in both Fourier images, (3) overestimation at $\lambda = 0.9$, and (4) a noise-free solution at $\lambda = 2$, consistent with the maximum values set by the Fourier methods.

IV. CONCLUSIONS

In conclusion, we present a thorough comparison between Fourier-based and Bayesian reconstruction algorithms using synthetic data with simulated noise models and experimental data obtained from wide-field N-*V* diamond magnetometry. Our findings indicate that, when only out-of-plane magnetic field data are available, the Bayesian method outperforms the out-of-plane Fourier method in several regimes. This superiority stems from the Bayesian method's systematic noise rejection and ability to reconstruct the underlying density with high resolution. Conversely, the out-of-plane Fourier method tends to incorporate sensing noise into the reconstruction outside the wire, displaying edge artifacts. In the realm of vector magnetometry, the in-plane Fourier method yields optimal reconstructions under low standoffs and moderate noise conditions. However, the Bayesian algorithm proves advantageous in scenarios involving high standoffs and/or substantial noise, delivering accurate current density magnitudes and sharp resolution. We have outlined a method for selecting the regularizer strength λ based on a rough understanding of the typical standoff in an experiment. This approach has resulted in physically accurate reconstructions with correct total currents and minimal aberrations. This work establishes a foundation for applying recently proposed Bayesian algorithms to magnetic fields acquired in a standard wide-field N-*V* center quantum diamond microscope. Additionally, it extensively discusses the limitations associated with existing Fourier methods.

ACKNOWLEDGMENTS

K.S. acknowledges funding from AOARD Grant No. FA2386-23-1-4012, DST-QuEST Grant No. DST/ICPS/QuST/Theme-2/2019/Q-58 and DST-SERB Power Grant No. SPG/2023/000063. K.S. acknowledges support from the IITB Nanofabrication facility. S.M. acknowledges funding from an I-Hub Chanakya Undergraduate Fellowship. D.A.B. and J.-P.T. acknowledge support by the Australian Research Council (ARC) through Grants Nos. FT200100073, DP220100178, and DE230100192.

[1] D. Vasyukov, Y. Anahory, L. Embon, D. Halbertal, J. Cuppens, L. Neeman, A. Finkler, Y. Segev, Y. Myasoedov, M. L. Rappaport, M. E. Huber, and E. Zeldov, A scanning superconducting quantum interference device with single electron spin sensitivity, Nat. Nanotechnol. **8**, 639 (2013).

[2] R. Monaco, C. Granata, R. Russo *et al.*, Superconducting flux-flow type ultra-low-noise magnetic sensors—An alternative to dc-squids, arXiv:1304.5761.

[3] R. Monaco, Magnetic sensors based on long Josephson tunnel junctions, Supercond. Sci. Technol. **25**, 115011 (2012).

[4] D. Budker and M. Romalis, Optical magnetometry, Nat. Phys. **3**, 227 (2007).

[5] M. Padniuk, M. Kopciuch, R. Cipolletti, A. Wickenbrock, D. Budker, and S. Pustelny, Response of atomic spin-based sensors to magnetic and nonmagnetic perturbations, Sci. Rep. **12**, 324 (2022).

[6] T. Ruster, H. Kaufmann, M. A. Luda, V. Kaushal, C. T. Schmiegelow, F. Schmidt-Kaler, and U. G. Poschinger, Entanglement-based dc magnetometry with separated ions, Phys. Rev. X **7**, 031050 (2017).

[7] S. Kotler, N. Akerman, Y. Glickman, A. Keselman, and R. Ozeri, Single-ion quantum lock-in amplifier, Nature **473**, 61 (2011).

[8] F. Casola, T. van der Sar, and A. Yacoby, Probing condensed matter physics with magnetometry based on nitrogen-vacancy centres in diamond, Nat. Rev. Mater. **3**, 17088 (2018).

[9] S. Scholten, A. Healey, I. Robertson, G. Abrahams, D. Broadway, and J.-P. Tetienne, Widefield quantum microscopy with nitrogen-vacancy centers in diamond:

Strengths, limitations, and prospects, J. Appl. Phys. **130**, 150902 (2021).
[10] E. V. Levine, M. J. Turner, P. Kehayias, C. A. Hart, N. Langellier, R. Trubko, D. R. Glenn, R. R. Fu, and R. L. Walsworth, Principles and techniques of the quantum diamond microscope, Nanophotonics **8**, 1945 (2019).
[11] R. Schirhagl, K. Chang, M. Loretz, and C. L. Degen, Nitrogen-vacancy centers in diamond: Nanoscale sensors for physics and biology, Annu. Rev. Phys. Chem. **65**, 83 (2014).
[12] A. Gruber, A. Dräbenstedt, C. Tietz, L. Fleury, J. Wrachtrup, and C. von Borczyskowski, Scanning confocal optical microscopy and magnetic resonance on single defect centers, Science **276**, 2012 (1997).
[13] J. Zhang and D. Suter, Single NV centers as sensors for radio-frequency fields, Phys. Rev. Res. **5**, L022026 (2023).
[14] M. Garsi, R. Stöhr, A. Denisenko, F. Shagieva, N. Trautmann, U. Vogl, B. Sene, F. Kaiser, A. Zappe, R. Reuter, and J. Wrachtrup, Three-dimensional imaging of integrated-circuit activity using quantum defects in diamond, Phys. Rev. Appl. **21**, 014055 (2024).
[15] J. L. Webb, L. Troise, N. W. Hansen, L. F. Frellsen, C. Osterkamp, F. Jelezko, S. Jankuhn, J. Meijer, K. Berg-Sørensen, J.-F. Perrier, A. Huck, and U. L. Andersen, High-speed wide-field imaging of microcircuitry using nitrogen vacancies in diamond, Phys. Rev. Appl. **17**, 064051 (2022).
[16] A. Nowodzinski, M. Chipaux, L. Toraille, V. Jacques, J.-F. Roch, and T. Debuisschert, Nitrogen-vacancy centers in diamond for current imaging at the redistributive layer level of integrated circuits, Microelectron. Reliab. **55**, 1549 (2015).
[17] S. E. Lillie, N. Dontschuk, D. A. Broadway, D. L. Creedon, L. C. Hollenberg, and J.-P. Tetienne, Imaging graphene field-effect transistors on diamond using nitrogen-vacancy microscopy, Phys. Rev. Appl. **12**, 024018 (2019).
[18] J.-P. Tetienne, N. Dontschuk, D. A. Broadway, A. Stacey, D. A. Simpson, and L. C. L. Hollenberg, Quantum imaging of current flow in graphene, Sci. Adv. **3**, e1602429 (2017).
[19] D. A. Broadway, S. C. Scholten, C. Tan, N. Dontschuk, S. E. Lillie, B. C. Johnson, G. Zheng, Z. Wang, A. R. Oganov, S. Tian, C. Li, H. Lei, L. Wang, L. C. L. Hollenberg, and J.-P. Tetienne, Imaging domain reversal in an ultrathin van der Waals ferromagnet, Adv. Mater. **32**, 2003314 (2020).
[20] D. Shishir and K. Saha, Nitrogen vacancy centre-based diamond microscope for investigating quantum materials, Bull. Mater. Sci. **44**, 276 (2021).
[21] J. L. Webb, L. Troise, N. W. Hansen, J. Achard, O. Brinza, R. Staacke, M. Kieschnick, J. Meijer, J.-F. Perrier, K. Berg-Sørensen, A. Huck, and U. L. Andersen, Optimization of a diamond nitrogen vacancy centre magnetometer for sensing of biological signals, Front. Phys. **8**, 522536 (2020).
[22] M. Parashar, A. Bathla, D. Shishir, A. Gokhale, S. Bandyopadhyay, and K. Saha, Sub-second temporal magnetic field microscopy using quantum defects in diamond, Sci. Rep. **12**, 8743 (2022).
[23] B. J. Roth, N. G. Sepulveda, and J. P. Wikswo, Using a magnetometer to image a two-dimensional current distribution, J. Appl. Phys. **65**, 361 (1989).
[24] D. Broadway, S. Lillie, S. Scholten, D. Rohner, N. Dontschuk, P. Maletinsky, J.-P. Tetienne, and L. Hollenberg, Improved current density and magnetization reconstruction through vector magnetic field measurements, Phys. Rev. Appl. **14**, 024076 (2020).
[25] F. Ghasemifard, M. Johansson, and M. Norgren, Current reconstruction from magnetic field using spherical harmonic expansion to reduce impact of disturbance fields, Inverse Probl. Sci. Eng. **25**, 795 (2017).
[26] D. M. Feldmann, Resolution of two-dimensional currents in superconductors from a two-dimensional magnetic field measurement by the method of regularization, Phys. Rev. B **69**, 144515 (2004).
[27] R. Kress, L. Kühn, and R. Potthast, Reconstruction of a current distribution from its magnetic field, Inverse Probl. **18**, 1127 (2002).
[28] A. Y. Meltzer, E. Levin, and E. Zeldov, Direct Reconstruction of two-dimensional currents in thin films from magnetic-field measurements, Phys. Rev. Appl. **8**, 064030 (2017).
[29] S. Tan, B. J. Roth, and J. P. Wikswo, The magnetic field of cortical current sources: The application of a spatial filtering model to the forward and inverse problems, Electroencephalogr. Clin. Neurophysiol. **76**, 73 (1990).
[30] R. J. Wijngaarden, H. J. W. Spoelder, R. Surdeanu, and R. Griessen, Determination of two-dimensional current patterns in flat superconductors from magneto-optical measurements: An efficient inversion scheme, Phys. Rev. B **54**, 6742 (1996).
[31] C. B. Clement, J. P. Sethna, and K. C. Nowack, Reconstruction of current densities from magnetic images by bayesian inference, arXiv:1910.12929.
[32] See Supplemental Material http://link.aps.org/supplemental/10.1103/PhysRevApplied.22.014015 for details on the simulation method (Sec. I), reconstruction algorithms (Sec. II), error estimation (Sec. III), regularizer selection (Sec. IV) and details of the experiments (Sec. V). The Supplemental Material also contains Refs. [41–45] (2024).
[33] Z. Wang, A. C. Bovik, H. R. Sheikh, and E. P. Simoncelli, Image quality assessment: From error visibility to structural similarity, IEEE Trans. Image Process. **13**, 600 (2004).
[34] S. Ontañón, An overview of distance and similarity functions for structured data, arXiv:2002.07420.
[35] A. Botchkarev, A new typology design of performance metrics to measure errors in machine learning regression algorithms, Interdiscip. J. Inf., Knowl., Manag. **14**, 045 (2019).
[36] D. S. Kalra and M. Barkeshli, in *Advances in Neural Information Processing Systems*, edited by A. Oh, T. Naumann, A. Globerson, K. Saenko, M. Hardt, and S. Levine (Curran Associates, Inc., 2023), Vol. 36, pp. 51621-51662, https://proceedings.neurips.cc/paper_files/paper/2023/file/a23598416361c7a9860164155e6ddd0b-Paper-Conference.pdf.
[37] P. C. Hansen, The *L*-curve and its use in the numerical treatment of inverse problems (2001), Vol. 4, pp. 119–142.
[38] S. Kindermann and K. Raik, A simplified *L*-curve method as error estimator, ETNA - Electron. Trans. Numer. Anal. **53**, 217 (2020).

[39] V. Agarwal, Total variation regularization and *L*-curve method for the selection of regularization parameter, ECE599 **21**, 1 (2003).

[40] V. V. Estrela, H. A. Magalhães, and O. Saotome, in *Advances in Computational Intelligence and Robotics* (IGI Global, 2016), p. 41.

[41] G. H. Golub, P. C. Hansen, and D. P. O'Leary, Tikhonov regularization and total least squares, SIAM J. Matrix Anal. Appl. **21**, 185 (1999).

[42] E. V. Levine, M. J. Turner, P. Kehayias, C. A. Hart, N. Langellier, R. Trubko, D. R. Glenn, R. R. Fu, and R. L. Walsworth, Principles and techniques of the quantum diamond microscope, Nanophotonics **8**, 1945 (2019).

[43] S. E. Lillie, D. A. Broadway, N. Dontschuk, S. C. Scholten, B. C. Johnson, S. Wolf, S. Rachel, L. C. L. Hollenberg, and J.-P. Tetienne, Laser modulation of superconductivity in a cryogenic wide-field nitrogen-vacancy microscope, Nano Lett. **20**, 1855 (2020).

[44] J.-P. Tetienne, N. Dontschuk, D. A. Broadway, S. E. Lillie, T. Teraji, D. A. Simpson, A. Stacey, and L. C. L. Hollenberg, Apparent delocalization of the current density in metallic wires observed with diamond nitrogen-vacancy magnetometry, Phys. Rev. B **99**, 014436 (2019).

[45] S. Boyd, N. Parikh, E. Chu, B. Peleato, and J. Eckstein *et al.*, Distributed optimization and statistical learning via the alternating direction method of multipliers, Foundations and Trends® in Machine learning **3** (1), 1 (2011).